


## RESEARCH ARTICLE

# A fast and novel method for amide proton transfer-chemical exchange saturation transfer multislice imaging

Jan-Rüdiger Schüre<sup>1</sup>  | Ulrich Pilatus<sup>1</sup> | Ralf Deichmann<sup>2</sup> | Elke Hattingen<sup>1</sup> | Manoj Shrestha<sup>2</sup>

<sup>1</sup>Department of Neuroradiology, University Hospital Frankfurt, Frankfurt am Main, Germany

<sup>2</sup>Brain Imaging Center (BIC), Goethe University Frankfurt, Frankfurt am Main, Germany

## Correspondence

Jan-Rüdiger Schüre, Department of Neuroradiology, University Hospital Frankfurt, Schleusenweg 2-16, Haus 95, 60528 Frankfurt am Main, Germany.

Email: jan-ruediger.schuere@kgu.de

Amide proton transfer-chemical exchange saturation transfer (APT-CEST) imaging provides important information for the diagnosis and monitoring of tumors. For such analysis, complete coverage of the brain is advantageous, especially when registration is performed with other magnetic resonance (MR) modalities, such as MR spectroscopy (MRS). However, the acquisition of Z-spectra across several slices via multislice imaging may be time-consuming. Therefore, in this paper, we present a new approach for fast multislice imaging, allowing us to acquire 16 slices per frequency offset within 8 s. The proposed fast CEST-EPI sequence employs a presaturation module, which drives the magnetization into the steady-state equilibrium for the first frequency offset. A second module, consisting of a single CEST pulse (for maintaining the steady-state) followed by an EPI acquisition, passes through a loop to acquire multiple slices and adjacent frequency offsets. Thus, the whole Z-spectrum can be recorded much faster than the conventional saturation scheme, which employs a presaturation for each single frequency offset. The validation of the CEST sequence parameters was performed by using the conventional saturation scheme. Subsequently, the proposed and a modified version of the conventional CEST sequence were compared in vitro on a phantom with different T1 times and in vivo on a brain tumor patient. No significant differences between both sequences could be found in vitro. The in vivo data yielded almost identical MTR<sub>asym</sub> contrasts for the white and gray matter as well as for tumor tissue. Our results show that the proposed fast CEST-EPI sequence allows for rapid data acquisition and provides similar CEST contrasts as the modified conventional scheme while reducing the scanning time by approximately 50%.

## KEYWORDS

amide proton transfer, APT-CEST, CEST EPI, echo planar imaging, MTR<sub>asym</sub>, multislice imaging, pH

**Abbreviations used:** APT, amide proton transfer; CEST, chemical exchange saturation transfer; CSF, cerebrospinal fluid; EPI, echo planar imaging; FoV, field of view; GM, gray matter; MTR<sub>asym</sub>, magnetization transfer ratio asymmetry; PVE, partial volume effect; RF, radiofrequency; SS, steady state; WM, white matter.

This is an open access article under the terms of the Creative Commons Attribution-NonCommercial License, which permits use, distribution and reproduction in any medium, provided the original work is properly cited and is not used for commercial purposes.

© 2021 The Authors. *NMR in Biomedicine* published by John Wiley & Sons Ltd.

## 1 | INTRODUCTION

Amide proton transfer-chemical exchange saturation transfer (APT-CEST) represents a technique for the imaging of low-concentration compounds with exchangeable protons that provides a sensitive contrast towards the intracellular pH ( $\text{pH}_i$ ), but also contain information about protein and peptide concentrations.<sup>1–6</sup>

In a previous study, different APT-CEST metrics were compared with  $\text{pH}_i$  maps, generated via  $^{31}\text{P}$ -MRS to verify the pH dependence of the APT contrast.<sup>7</sup> To achieve a combined evaluation between both magnetic resonance (MR) modalities across several slices, sufficient coverage of the brain is required for CEST imaging to improve the coregistration. Since the acquisition of a full Z-spectrum is time-consuming, especially when several slices are recorded, different approaches have been proposed for clinical investigations, which allow the acquisition of CEST data in a clinically acceptable time, such as the acquisition of a few selected frequency offsets<sup>8</sup> or the implementation of keyhole techniques.<sup>9</sup> Another previous study modified the conventional multislice CEST sequence to shorten scanning time by dividing the radiofrequency (RF) irradiation scheme into a long and a short module.<sup>10</sup> While the long RF saturation module drives the magnetization into the steady state, the repetitive short RF irradiation module maintains the CEST contrast for multislice acquisition and measurement repetitions for a specific frequency offset. It could be demonstrated that this scheme provides almost identical CEST contrasts as a conventional multislice CEST technique, where one long RF-irradiation module is used for the acquisition of each slice.

However, this scheme is still time-consuming due to the insertion of regular presaturation delays (for relaxation recovery) and the long primary saturation module prior to each new frequency offset. In this study, we modify the method of Sun et al.<sup>10</sup> and propose two schemes (dubbed “CEST<sub>SS</sub>” and “CEST<sub>fast</sub>”) that maintain the CEST contrast for multislice imaging. While the steady-state scheme (CEST<sub>SS</sub>) is similar to the sequence presented by Sun et al.,<sup>10</sup> the CEST<sub>fast</sub> sequence represents a new approach, which applies the long saturation module only for the first frequency offset and thus saves almost half of the measurement time. Both sequences were compared in vitro and in vivo.

## 2 | MATERIALS AND METHODS

### 2.1 | Phantom and subjects

A cylindrical phantom containing three 50-mL Falcon tubes was prepared for sequence comparison. Each tube contained a phosphate buffer solution doped with sodium chloride (NaCl) and 10 g of edible gelatin to provide proteins for the required CEST effect. In addition, all the tubes were set to different T1 values of approximately 450, 850 and 1300 ms by adapting the concentration of Gadovist, as described previously.<sup>11,12</sup> Before heating the solution in a microwave oven, the mixture in all tubes was stirred and the pH value was adjusted with a 1 mmol/L solution of potassium hydroxide (KOH) to achieve a pH of approximately 7.0. After the preparation, the pH values in the gelled state were measured via pH strips and readjusted with KOH after previous heating, if necessary.

For in vivo measurements, a patient with a brain tumor (glioblastoma) was scanned, applying both CEST sequences, as described in the next section. The study was approved by the local ethics committee of the University Hospital, and the subject gave written informed consent before scanning.

### 2.2 | CEST sequences

The acquisition of a Z-spectrum requires the readout of the longitudinal magnetization after sufficient saturation via RF pulses with different frequency offsets. These offsets usually cover a range of several ppm symmetrically around the water signal. In our previous work, we applied a train of rectangular RF pulses with a total duration of 8 s prior to each single-slice echo-planar imaging (EPI) readout, which was repeated for several frequency offsets.<sup>7</sup> A similar scheme was used by Sun et al.<sup>13</sup> on a 4.7-T animal scanner, acquiring several consecutive EPI slices after the saturation period to obtain multislice data. However, this approach requires additional postprocessing to correct for the relaxation-induced loss of CEST contrast for each slice. Sun et al. further showed that a short additional saturation period for every single slice is sufficient to maintain a steady-state saturation, thus avoiding the requirement of a slice-specific correction via postprocessing.<sup>10</sup> Based on these findings, we designed the steady-state CEST-EPI (CEST<sub>SS</sub>) sequence (Figure 1A). The schematic representation shows an initial CEST saturation module (red) and an acquisition module (black).

The CEST saturation module executes repetitively a basic module, consisting of a single rectangular pulse of duration  $\delta$ , followed by a delay time of equal duration. The delay further includes a spoiler gradient (S) to disperse transverse magnetization and a fat suppression (FS) module. Assuming that FS does not interfere with the CEST saturation, repetitive application of this basic module can be used for establishing the steady-state magnetization for CEST imaging. Thus, the module is embedded in a dummy scan loop with  $N_{\text{dummy}}$  repetitions, using for each RF pulse a constant amplitude of  $B_1$ , which is sufficient to achieve the steady-state CEST contrast at a defined frequency offset ( $\omega$ ).

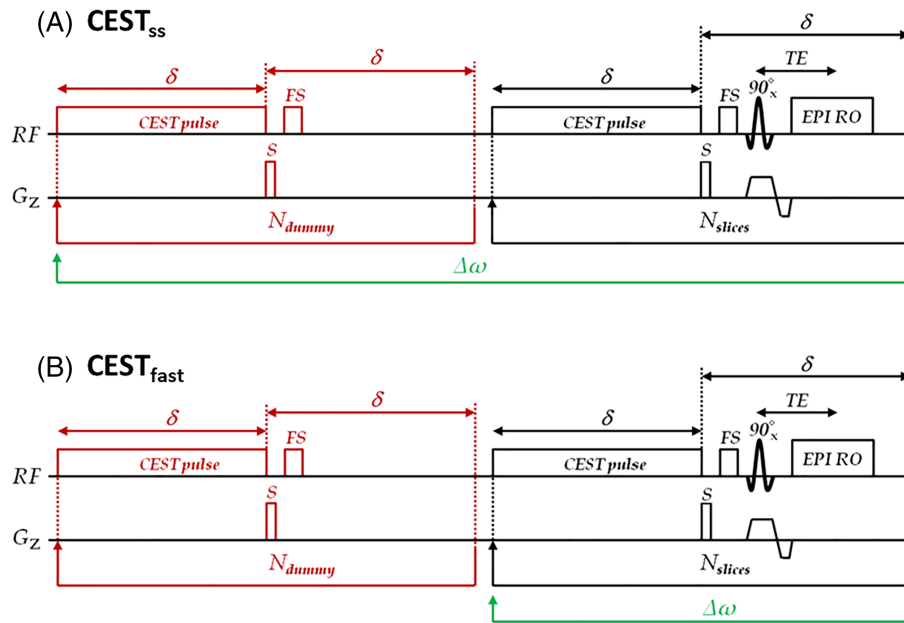


**FIGURE 1** Schematic depiction of the multislice chemical exchange saturation transfer (CEST) sequences ( $\text{CEST}_{\text{ss}}$  and  $\text{CEST}_{\text{fast}}$ ) with echo-planar imaging (EPI) acquisition. A, The steady-state CEST-EPI sequence employs a basic module embedded in a loop to achieve a sufficient number of dummy scans ( $N_{\text{dummy}}$ ) to generate a steady-state saturation prior to each volume of data acquisition (CEST saturation module [red]). Each repetition of the dummy loop contains a single rectangular pulse of duration  $\delta$  and a spoiler gradient  $S$  to disperse transverse magnetization, followed by a fat suppression (FS) module. The subsequent multislice acquisition module (black) comprises a single rectangular pulse followed by  $S$ , FS and an EPI readout within a slice loop ( $N_{\text{slices}}$ ). Both loops ( $N_{\text{dummy}}$  and  $N_{\text{slices}}$ ) are repeated for each new frequency offset ( $\omega$ ). B, The proposed fast CEST-EPI sequence is similar to A except for different positioning of the frequency offset loop. In detail, the CEST saturation module is only performed once at the beginning for the first frequency offset. This initial dummy scan drives the magnetization into a steady state, which is then maintained throughout the  $N_{\text{slices}}$  and  $\Delta\omega$  loops with the acquisition module

The acquisition module is similar to the basic module but includes a single-slice EPI readout after the FS in the delay. It is important to note that the modified delay with the inserted EPI readout has the same duration  $\delta$  as the delay in the basic module, so timings in both modules (CEST saturation and acquisition) are identical, thus maintaining the steady state. Multislice imaging is achieved by embedding the acquisition module in a slice loop ( $N_{\text{slices}}$ ) while maintaining the steady-state magnetization with a single RF saturation pulse.

In the  $\text{CEST}_{\text{ss}}$  sequence (Figure 1A), both the CEST saturation module and the subsequent acquisition module are repeated in a frequency offset loop, that is, for each frequency offset  $\omega$ , the basic module is repeated  $N_{\text{dummy}}$  times before multislice imaging is performed with the acquisition module across  $N_{\text{slices}}$  at the same  $\omega$ . Phase and read encodings are not shown in the figure for the sake of clarity.

To shorten the scanning time, the steady-state sequence is modified, as shown in the proposed scheme for the fast CEST-EPI ( $\text{CEST}_{\text{fast}}$ ) sequence (Figure 1B). Here, only the acquisition module is embedded in the frequency offset loop (i.e. the initial CEST saturation module is applied only for the first frequency offset to achieve the steady-state frequency-selective saturation). This is based on the assumption that the saturation pulse in the acquisition module is sufficient to maintain the steady state, provided the difference between subsequent values of  $\omega$  is small and does not exceed 0.5 ppm (approximately 60 Hz). Thus, the acquisition module can be executed continuously for all slices and adjacent frequency offsets.

In this study, the  $\text{CEST}_{\text{ss}}$  sequence was used as a reference method and compared with the proposed  $\text{CEST}_{\text{fast}}$  sequence. The number of saturation pulses, as well as the irradiation power  $B_1$ , were varied to achieve the optimal values for improving the saturation efficiency  $\alpha$ . The corresponding results are presented in the supporting information (Figures S.1–S.3). In addition, the Z-spectra of the multislice  $\text{CEST}_{\text{fast}}$  sequence were simulated based on an analytical solution of the Bloch–McConnell equations. The Matlab code is provided by the project “CEST sources”, which is available under <https://www.cest-sources.org>. The corresponding calculation of the longitudinal relaxation rate in the rotating frame can be found in the work of Zaiss and Bachert.<sup>14</sup> The modification and results of the simulation are shown in the supporting information.

### 2.3 | MRI experiments

Experiments were performed on a 3-T whole-body MRI system (MAGNETOM Prisma; Siemens Healthineers, Erlangen, Germany) using a body transmit and a 20-channel phase-array head/neck receive coil.

$T_1$  mapping was based on the variable flip angle (VFA) method,<sup>15–17</sup> for which two three-dimensional RF-spoiled gradient echo (GE) datasets with different excitation angles ( $FA_1$ ,  $FA_2$ ) were acquired. The following image parameters were used: isotropic spatial resolution of  $1 \times 1 \times 1 \text{ mm}^3$ , field of view (FoV) =  $256 \times 224 \times 160 \text{ mm}^3$ , TR/TE/ $FA_1/FA_2$  =  $16.4/6.7 \text{ ms}/4^\circ/24^\circ$ , bandwidth =  $222 \text{ Hz/pixel}$ . To correct  $T_1$  for  $B_1$  inhomogeneities, two additional datasets were acquired using two-dimensional GE with and without magnetization preparation via a  $45^\circ$  RF pulse.<sup>18</sup>

For assessment of the tumor anatomy,  $T_2$ -weighted turbo spin echo (TSE) data were acquired with: TE/TR =  $102/4920 \text{ ms}$ , FoV =  $192 \times 192 \text{ mm}^2$ , echo spacing =  $16.9 \text{ ms}$ , spatial resolution =  $1.5 \times 1.5 \times 3 \text{ mm}^3$  and 25 slices.

For APT-CEST imaging, the two sequences (CEST<sub>SS</sub>, CEST<sub>fast</sub>) as described above were employed. Sequence parameters related to the saturation were optimized on a phantom with the CEST<sub>SS</sub> sequence (as described in the supporting information), resulting in a rectangular pulse with  $B_1 = 1 \mu\text{T}$ , duration  $\delta = 250 \text{ ms}$  and  $N_{\text{dummy}} = 16$  for 8 s. The Z-spectra were acquired in the range from  $-8$  to  $+8 \text{ ppm}$  relative to the water signal according to the following scheme:

1. Unsaturated reference scan (CEST<sub>SS</sub>: 1 min 4 s; CEST<sub>fast</sub>: 40 s).
2. The entire range with an increment of 0.5 ppm (CEST<sub>SS</sub>: 8 min 48 s; CEST<sub>fast</sub>: 4 min 32 s).
3. The spectral range from  $-4$  to  $-3 \text{ ppm}$  with an increment of 0.1 ppm (CEST<sub>SS</sub>: 2 min 58 s; CEST<sub>fast</sub>: 1 min 36 s).
4. The spectral range from  $+3$  to  $+4 \text{ ppm}$  with an increment of 0.1 ppm (CEST<sub>SS</sub>: 2 min 58 s; CEST<sub>fast</sub>: 1 min 36 s).

Each step was performed twice successively, using two different echo times ( $TE_1$ ,  $TE_2$ ) in the acquisition module and recording magnitude and phase data to perform a Dixon correction for the suppression of lipid artifacts in the EPI data.<sup>19</sup> A reference image ( $S_0$ ) without RF irradiation ( $B_1 = 0 \mu\text{T}$ ) was acquired additionally (an average of four measurement repetitions). Parameters for the image acquisition module were:  $TE_1 = 22.08 \text{ ms}$ ,  $TE_2 = 23.28 \text{ ms}$ , TR = 8 s, FoV =  $192 \times 192 \text{ mm}^2$ , in-plane resolution =  $3 \times 3 \text{ mm}^2$ , 16 axial slices with thickness = 4 mm, interslice gap = 1 mm, echo spacing = 0.5 ms, readout bandwidth =  $2298 \text{ Hz/pixel}$ .

Phantom and patient data were acquired using the CEST<sub>SS</sub> and the proposed CEST<sub>fast</sub> sequence. To exclude a potential bias in the CEST<sub>SS</sub> results induced by incomplete spin relaxation after completion of the acquisition module and switching to the next frequency offset  $\omega$ , the in vitro study was repeated with the second version of the CEST<sub>SS</sub> sequence, adding a relaxation delay of 10 s before each CEST basic module. The following table shows the total measurement times for in vitro and in vivo imaging to the proposed acquisition scheme with 55 offsets, including two measurement repetitions according to each echo time.

	Measurement time CEST <sub>SS</sub>	Measurement time CEST <sub>fast</sub>	Total measurement time
in vitro/ in vivo	31 min 36 s	16 min 48 s	48 min 24 s

While the acquisition of a volume with 16 slices via CEST<sub>SS</sub> takes 16 s, the CEST<sub>fast</sub> requires the same time only for the first frequency offset of a run. For each subsequent frequency offset, the time is reduced to 8 s, which corresponds to a time saving of almost 50%.

## 2.4 | Postprocessing

Image processing was performed in MATLAB (MathWorks, Natick, MA, USA) and with the software FSL version 6.0.1.<sup>20</sup>

First, EPI data were corrected for lipid artifacts by voxelwise addition of the complex (phase and magnitude) image data recorded with different TE, where the signals of water and fat are in-phase ( $TE_1$ ) and  $180^\circ$  out-of-phase ( $TE_2$ ).<sup>21</sup> Afterwards, all images were sorted according to the saturation frequency and merged along the fourth dimension for motion correction via FLIRT,<sup>22</sup> followed by brain extraction (for in vivo data) via BET.<sup>23</sup> The resulting images were divided by the motion-corrected and averaged reference dataset  $S_0$ . Subsequently, Z-spectra were fitted with an inverted Lorentzian function from  $\omega = -1$  to  $+1 \text{ ppm}$ , to detect the center of each Z-spectrum with the lowest signal intensity according to Equation (1). The amplitude is given by A, while the full width at half maximum (FWHM) is represented by  $\Gamma$ . The chemical shift ( $\omega_0$ ) according to the frequency offset at 0 ppm was used for  $B_0$  correction by linear interpolation of the Z-spectra and shifting the offset axis based on the WASSR approach.<sup>24</sup>

$B_0$ -corrected Z-spectra ( $Z_{B_0}$ ) were analyzed assuming a four-pool model with a linear combination of inverted Lorentzian functions, fitting the signals of direct water saturation ( $L_{DS}$ ), semisolid MT ( $L_{MT}$ ), nuclear Overhauser effect (NOE) from aliphatic protons ( $L_{NOE}$ ) and amide protons ( $L_{Amide}$ ) (Equation 2). To ensure accurate fitting, starting parameters (SP), as well as lower and upper boundaries (LB/UB), were defined in advance for each pool according to their amplitude, FWHM, and chemical shift (Table 1). The Levenberg–Marquardt algorithm, as implemented in MATLAB's nonlinear curve fitting toolbox, was used to fit the data. A bisquare weighting was applied to reduce the impact of outliers on the fit. To assess the quality of the inverted Lorentzian fit, the root-mean-square error (RMSE) was calculated for each voxel and plotted on a parametric RMSE map. After fitting the whole Z-spectrum with a four-pool model, the asymmetry MT ratio ( $MTR_{\text{asym}}$ ) was calculated using Equation (3).

**TABLE 1** Listing of the starting parameters (SP) as well as lower and upper boundaries (LB/UB) for inverse Lorentzian fitting of the Z-spectra according to a four-pool model including the signals from direct water saturation, semisolid magnetization transfer (MT), amide protons and aliphatic nuclear Overhauser effect (NOE)

Pool	amplitude (A)			FWHM ( $\Gamma$ )			chemical shift ( $x_0$ )		
	LB	SP	UB	LB	SP	UB	LB	SP	UB
Direct saturation	0	0.9	1	1	1.4	3	-1	0	1
Semisolid MT	0	0.1	1	35	40	45	-3	-2.5	-2
Amide protons	0	0.01	0.3	0.3	0.5	3	3	3.5	4
Aliphatic NOE	0	0.01	0.4	0.3	3	5	-4	-3.5	-3

$$L(\omega) = 1 - \left( A * \frac{\Gamma^2}{\Gamma^2 + 4 * (\omega - \omega_0)^2} \right) \quad (1)$$

$$Z_{4\text{pool}} = L_{\text{DS}} + L_{\text{MT}} + L_{\text{Amide}} + L_{\text{NOE}} \quad (2)$$

$$\text{MTR}_{\text{asym}}(\Delta\omega) = Z_{4\text{pool}}(-\omega) - Z_{4\text{pool}}(+\omega). \quad (3)$$

For the in vitro experiments, a region of interest (ROI) analysis was performed. The ROI was placed around the center of each tube, covering eight slices. Mean values and standard deviations (SD) were obtained for each slice and the entire volume as part of the sequence comparison. To estimate the sensitivity of each sequence, the contrast-to-noise ratio (CNR) was calculated according to Equation (4), where Sa and Sb are the signal intensities from two different tubes and  $\sigma$  is the SD of the background noise.

$$\text{CNR} = \frac{S_a - S_b}{\sigma}. \quad (4)$$

The evaluation of the in vitro data yielded  $B_0$ -corrected Z-spectra and the calculated  $\text{MTR}_{\text{asym}}$  values.

For the in vivo experiments, ROIs and volumes of interest (VOIs) were generated from quantitative  $T_1$  ( $qT_1$ ) data. For  $qT_1$  mapping, the two GE datasets acquired at different flip angles were coregistered, subjected to brain extraction and tissue segmentation via BET<sup>23</sup> and FAST,<sup>25</sup> and processed as described in the literature to correct for insufficient RF spoiling<sup>15</sup> and  $B_1$  inhomogeneities.<sup>18</sup> Subsequently, the unsaturated CEST reference was coregistered to the  $T_1$  map with FLIRT,<sup>22</sup> employing the boundary-based registration via the white matter (WM) segmentation. Afterwards, the WM and gray matter (GM) probability maps, derived from the  $T_1$  map, were transferred back into the original space of the CEST data. For further evaluation, only voxels with a probability of at least 80% of belonging to the respective tissue type were considered. Additionally, a tumor VOI was defined by an experienced neuroradiologist based on the  $T_2$ -weighted image, which was subsequently coregistered to the CEST space with FLIRT.

Quantitative comparison of the  $\text{CEST}_{\text{SS}}$  and  $\text{CEST}_{\text{fast}}$  sequences was performed on a representative slice with tumor tissue, according to the parameterized maps from  $Z_{B_0}$  (+3.5 ppm),  $\text{MTR}_{\text{asym}}$  (3.5 ppm) and the RMSE. In addition, subtraction maps between the two sequences were calculated based on the parameterized maps for  $Z_{B_0}$  (+3.5 ppm) and  $\text{MTR}_{\text{asym}}$  (3.5 ppm). Furthermore, a slice-selective boxplot analysis was carried out within the WM, GM and tumor VOIs based on the calculated difference between both CEST-EPI sequences. Since the boxplots do not provide any local information, the unsaturated reference dataset as well as the previous subtraction map of  $\text{MTR}_{\text{asym}}$  (3.5 ppm) between both sequences are presented for all 16 slices. In a last step, the Pearson correlation and the Bland-Altman diagram were used to assess the agreement between both measurements. For this purpose, a ROI was drawn in the left and the right hemispheres, including WM, deeper GM and tumor tissue. In addition, a boxplot was added, showing the distribution of values for both sequences within the ROI for WM, GM and tumor tissue. Statistical analysis was performed in vitro and in vivo via paired T-tests.

### 3 | RESULTS

Figure 2 shows a comparison of the different Z-spectra for the in vitro experiment, acquired with the optimized parameters of the CEST saturation module ( $B_1 = 1 \mu\text{T}$ ,  $N_{\text{dummy}} = 16$ ), using the  $\text{CEST}_{\text{SS}}$  sequence with (blue) and without (red) the relaxation delay of 10 s, as well as the  $\text{CEST}_{\text{fast}}$  sequence (green). The results are shown separately for all three tubes with different  $T_1$ . For increasing  $T_1$ , the data show for all sequences a broadening of the Z-spectrum, a stronger saturation at the resonance frequency of water at 0 ppm and an elevated salience of the saturation peak in the spectral range of amide protons.

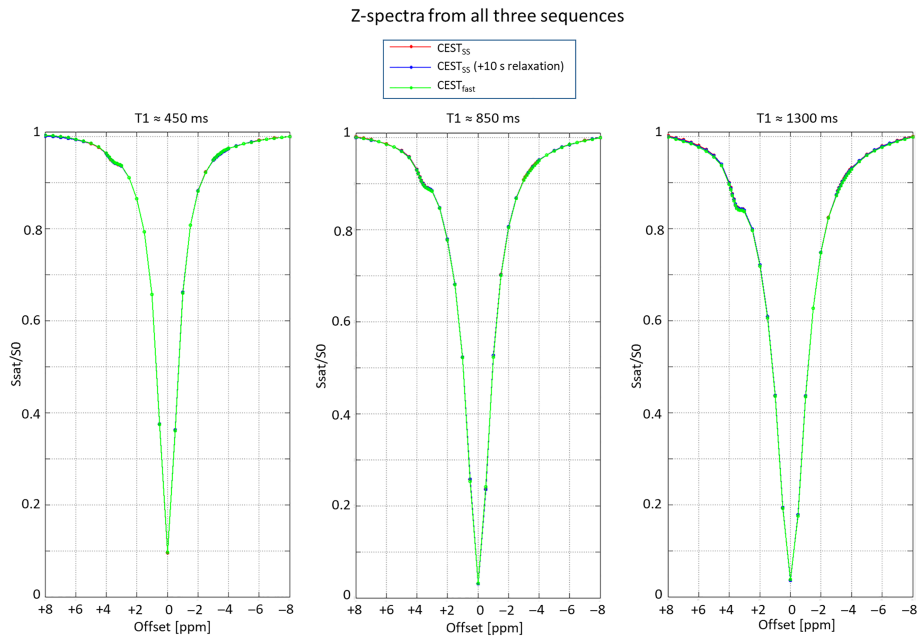


**FIGURE 2** Comparison of the  $B_0$ -corrected Z-spectra obtained with the proposed  $CEST_{fast}$  sequence (green), the  $CEST_{SS}$  with (blue) and without (red) the relaxation delay of 10 s. The spectra show very good agreement, independent from  $T_1$  (left:  $T_1 = 450$  ms, middle:  $T_1 = 850$  ms, right:  $T_1 = 1300$  ms)

**TABLE 2** Statistic parameters of  $Z_{B_0}$  (+3.5 ppm) for both the  $CEST_{SS}$  and  $CEST_{fast}$  sequences

$Z_{B_0}$ (3.5 ppm)	tube 1 ( $T_1 = 450$ ms)				tube 2 ( $T_1 = 850$ ms)				tube 3 ( $T_1 = 1300$ ms)			
	mean	std	min	max	mean	std	min	max	mean	std	min	max
$CEST_{SS}$	0.943	$\pm 0.005$	0.927	0.952	0.896	$\pm 0.005$	0.876	0.907	0.847	$\pm 0.008$	0.827	0.862
$CEST_{SS}$ (10 s)	0.943	$\pm 0.006$	0.927	0.952	0.895	$\pm 0.006$	0.878	0.908	0.846	$\pm 0.007$	0.83	0.862
$CEST_{fast}$	0.944	$\pm 0.006$	0.926	0.955	0.893	$\pm 0.006$	0.876	0.907	0.843	$\pm 0.008$	0.826	0.861

There is very good agreement between the Z-spectra obtained with the different sequences, independent from  $T_1$ . In particular, comparison of both  $CEST_{SS}$  data acquired with (blue) and without (red) the 10-s relaxation delay shows that omission of the delay does not affect the acquisition of subsequent frequency offsets. Furthermore, there is no significant difference between the data acquired with both  $CEST_{SS}$  and the  $CEST_{fast}$  sequence, which confirms the applicability of the proposed saturation scheme.

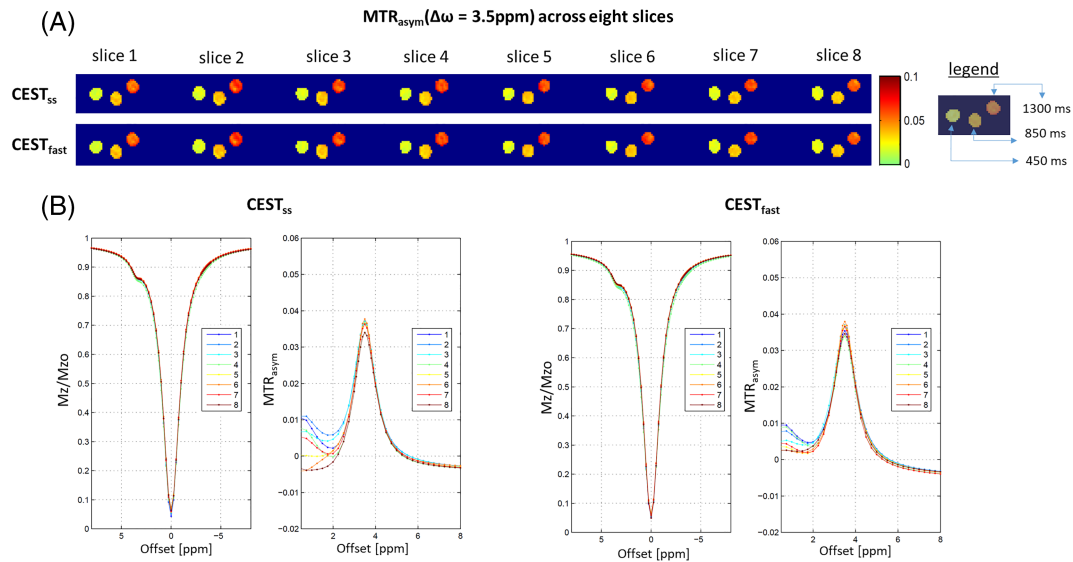
The data in Table 2 confirm these observations for  $Z_{B_0}$  (+3.5 ppm), showing that all sequences yield nearly equal values within the image noise level ( $\delta$ ) of  $0.005 = 0.5\%$ , which is in agreement with the measured SD within the VOI.

Figure 3A displays a comparison of the  $MTR_{asym}$  (3.5 ppm) maps across eight slices, based on in vitro data obtained with  $CEST_{SS}$  (top) and  $CEST_{fast}$  (bottom). The results show that both sequences yield similar contrasts for each  $T_1$ , which remain constant across the slices. The corresponding mean values and SD within the entire VOI are shown in Table 3 and confirm these observations.

Figure 3B shows Z-spectra and  $MTR_{asym}$  data for the tube with  $T_1 = 850$  ms overlaid for all slices (different colors), both for  $CEST_{SS}$  (left) and  $CEST_{fast}$  (right). Both sequences yield almost identical results with rather marginal differences between the slices. Concerning  $MTR_{asym}$ , minor differences can be found in the spectral range of  $\Delta\omega = 0-2$  ppm, which can be attributed to insufficient  $B_0$  correction. More details and further results for all three tubes are given in Table S.4. In summary, there is a high correlation between the  $MTR_{asym}$  (3.5 ppm) results obtained with  $CEST_{SS}$  and  $CEST_{fast}$  ( $r = 0.94$ ,  $p = .012$ ), as well as contrast consistency across all slices.

Figure 4 presents the in vivo results acquired on the glioblastoma patient for a representative slice comprising tumor tissue. Parameterized maps are displayed for  $Z_{B_0}$  (+3.5 ppm) (top row),  $MTR_{asym}$  (3.5 ppm) (central row) and the voxelwise corresponding RMSE (bottom row) for both sequences (left and central columns). In addition, subtraction maps for  $Z_{B_0}$  (+3.5 ppm) and  $MTR_{asym}$  (3.5 ppm) are shown (right column). Tumor location and further structural information are shown in the coregistered  $T_2$ -weighted image (bottom right).

$Z_{B_0}$  results across the WM, GM and tumor VOIs are similar for both sequences, yielding the values  $GM_{steady-state/fast} = 0.69 \pm 0.05/0.69 \pm 0.04$ ,  $WM_{steady-state/fast} = 0.71 \pm 0.04/0.71 \pm 0.05$ , and  $tumor_{steady-state/fast} = 0.72 \pm 0.03/0.72 \pm 0.02$ . However, the subtraction map



**FIGURE 3** A, Comparison of the parameterized  $MTR_{asym}$  (3.5 ppm) maps obtained with the modified steady-state ( $CEST_{SS}$ ) and the proposed fast CEST-EPI ( $CEST_{fast}$ ) sequences. Maps are shown for eight slices of the phantom tubes with three different  $T_1$  relaxation times (from left to right: 450, 850 and 1300 ms). B, Separate display of data for all slices from the tube with  $T_1 = 850$  ms, showing the  $B_0$  corrected Z-spectra ( $Z_{B_0}$ ) and  $MTR_{asym}$  data, both for  $CEST_{SS}$  (left) and  $CEST_{fast}$  (right)

**TABLE 3** Mean value and standard deviation of  $MTR_{asym}$  (3.5 ppm) within the VOI across eight slices for  $CEST_{SS}$  and the proposed  $CEST_{fast}$  sequence

	Tube 1	Tube 2	Tube 3
$CEST_{SS}$	$0.018 \pm 0.003$	$0.036 \pm 0.003$	$0.057 \pm 0.006$
$CEST_{fast}$	$0.016 \pm 0.003$	$0.036 \pm 0.003$	$0.057 \pm 0.006$

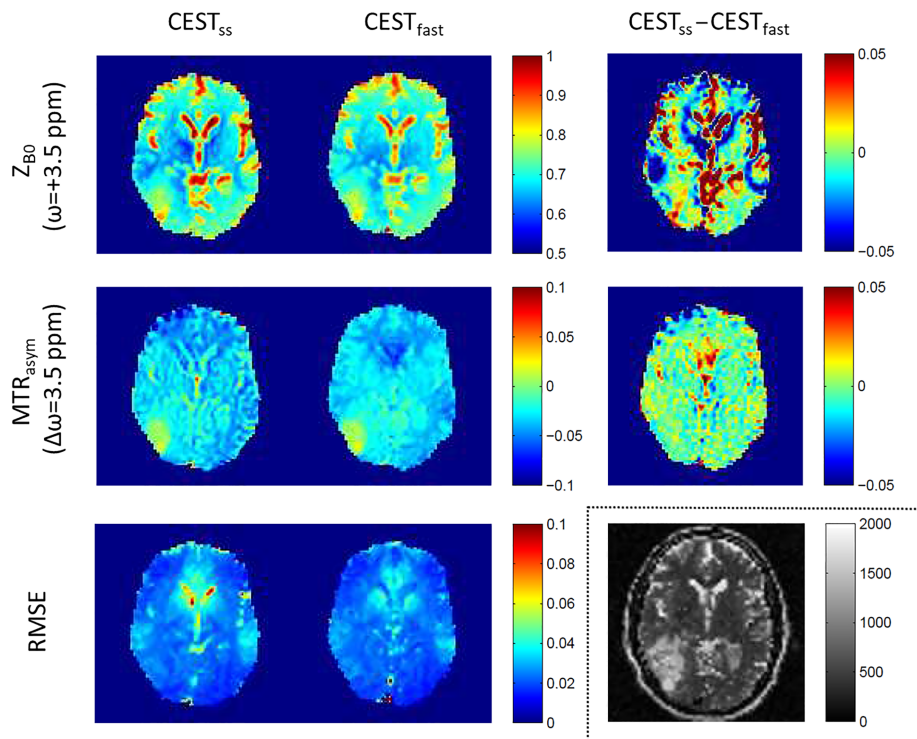


**FIGURE 4** Sequence comparison for data acquired on a glioblastoma patient showing parametrized maps of  $Z_{B_0}$  (+3.5 ppm) (top row),  $MTR_{asym}$  (3.5 ppm) (middle row) and the RMSE of the fitted Z-spectrum for each voxel (bottom row), for  $CEST_{SS}$  (left column) and  $CEST_{fast}$  (central column). The difference between both sequences is shown via the subtraction map for  $Z_{B_0}$  and  $MTR_{asym}$  (right column). A coregistered  $T_2$ -weighted turbo spin echo (TSE) image is shown for structural information (bottom right)

shows regional differences in the area of GM ( $\sim 0.01$ ) or parts of tumor tissue ( $\sim 0.05$ ), while larger differences of 0.1–0.16 were observed for ventricular and cortical cerebrospinal fluid (CSF). Those observations may be attributed to partial volume effects from components with rather long  $T_1$  or may arise from not fully relaxed equilibrium magnetization, due to the limited repetition time of 8 s.

For  $MTR_{asym}$ , regional differences are significantly reduced since all effects that are symmetric regarding the water frequency are canceled during the calculation. The remaining contrast, which includes the APT-CEST effect, clearly indicates the tumor area. Average values for each tissue VOI within the slice are similar between sequences ( $GM_{steady-state/fast} = -0.031 \pm 0.021 / -0.030 \pm 0.019$ ,  $WM_{steady-state/fast} = -0.043 \pm 0.016 / -0.041 \pm 0.013$ , and  $tumor_{steady-state/fast} = -0.014 \pm 0.009 / -0.010 \pm 0.011$ ). Consequently, the subtraction map shows relatively low residual differences, except for regions of cortical and ventricular CSF, as well as single voxels close to CSF compartments. In those areas, higher intensities of the RMSE maps indicate reduced fitting accuracy for the Z-spectra.

Figure 5A shows the difference between  $MTR_{asym}$  (3.5 ppm) values obtained with the  $CEST_{SS}$  and the  $CEST_{fast}$  sequences via a boxplot analysis covering the entire range of 16 slices. The corresponding subtraction map (Figure 5B) provides information about local differences between the results. The unsaturated reference dataset (Figure 5C) serves as a structural reference. Across all slices of the WM, GM and tumor VOIs, Figure 5A confirms that the median value of the differences between both sequences is almost zero (WM:  $-0.003 \pm 0.002$ , GM:  $-0.004 \pm 0.007$ , tumor:  $-0.002 \pm 0.002$ ). Furthermore, for all VOIs, no significant change in the mean values over the slices can be observed (WM/GM:  $p < .001$ /tumor:  $p = .008$ ). Regarding the distribution of the differences, a decrease of the interquartile range (IQR) can be observed from inferior to superior slices. While higher IQR can be detected for the WM and GM up to slice 4 ( $IQR_{WM \text{ slice } 1-4} \approx 0.014$ ,  $IQR_{GM \text{ slice } 1-4} \approx 0.011$ ), values are reduced and more homogeneous from slice 5 to 16 ( $IQR_{WM \text{ slice } 5-16} \approx 0.008$ ,  $IQR_{GM \text{ slice } 5-16} \approx 0.007$ ). Figure 5B confirms the increased difference between the results obtained with both sequences in the frontal brain regions, while Figure 5C indicates distortions in these areas due to higher field inhomogeneities, which correlate with the larger deviations. Concerning tumor tissue, lower IQR ( $IQR_{tumor \text{ slice } 4-11} \approx 0.006$ ) are revealed, corresponding to our findings via the subtraction map, in which the tumor is no longer visible.

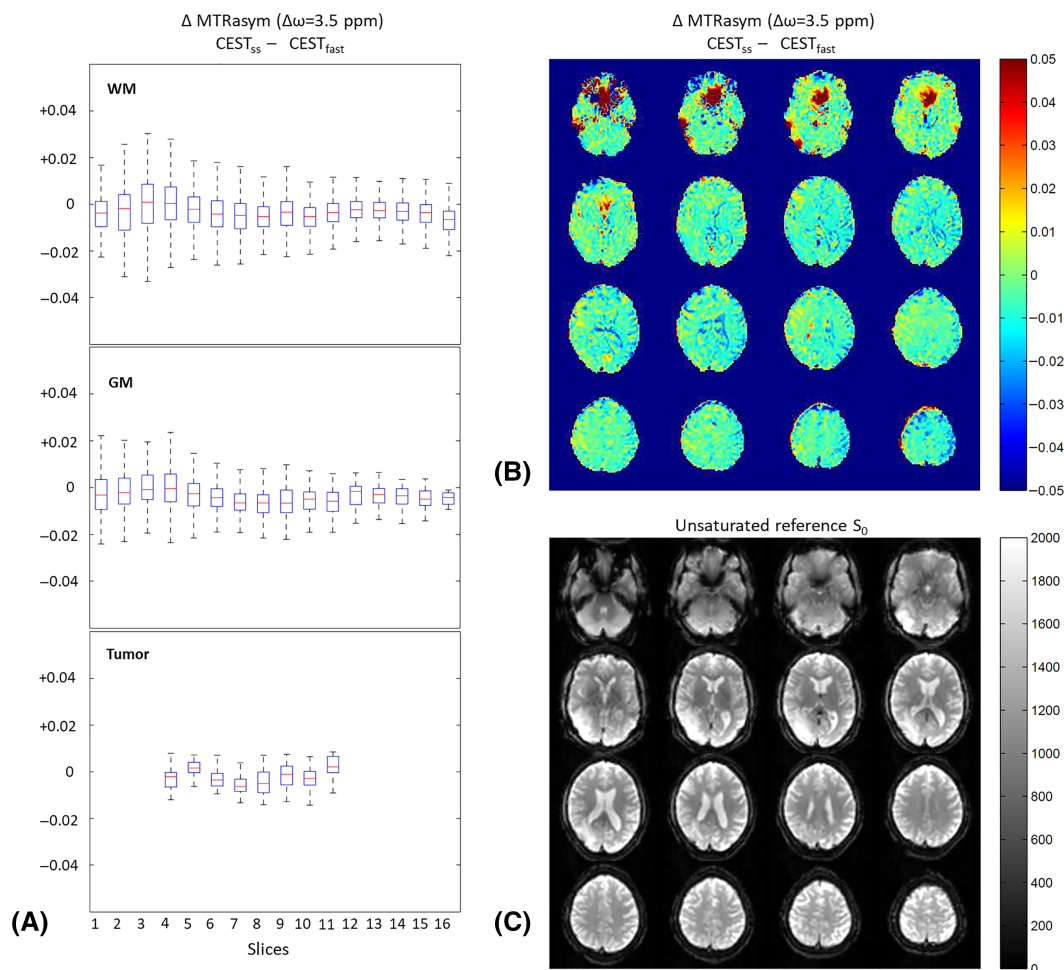


**FIGURE 5** A, Boxplot analysis of the difference between  $MTR_{asym}$  (3.5 ppm) values obtained with the  $CEST_{SS}$  and  $CEST_{fast}$  sequences for white matter (WM), gray matter (GM) and tumor tissue across all 16 slices. B, Corresponding subtraction map of  $MTR_{asym}$  (3.5 ppm), indicating differences between both sequences. C, Corresponding unsaturated reference dataset ( $S_0$ ) for structural information

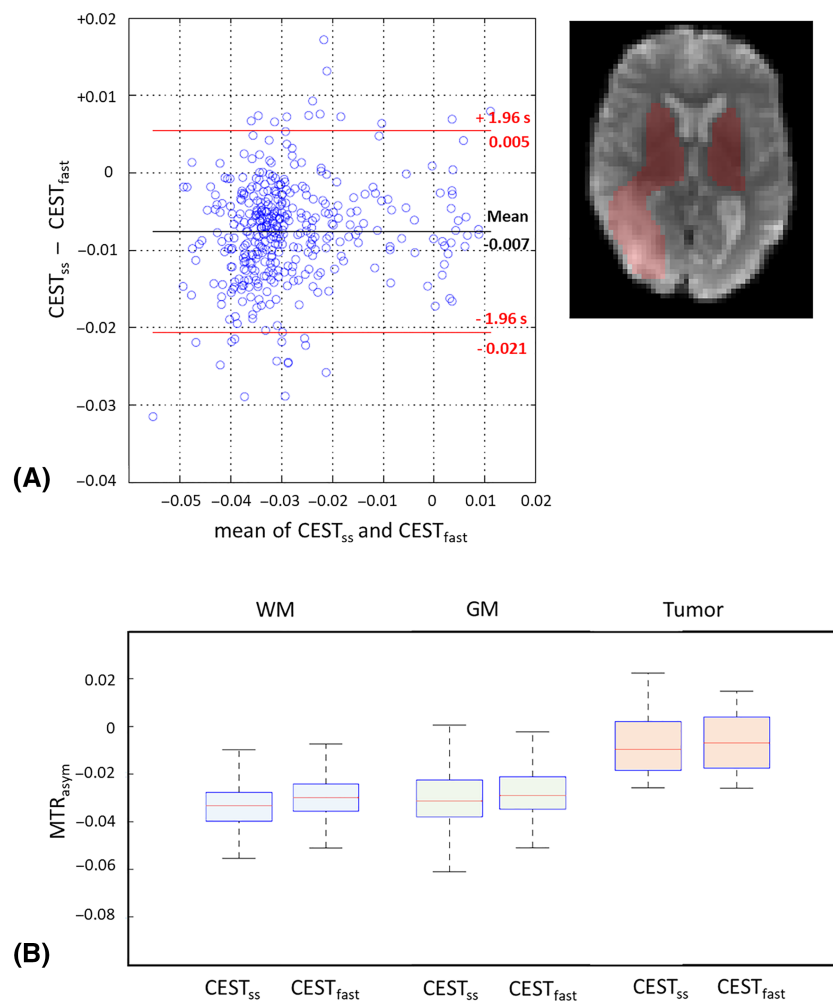


Figure 6A provides a sequence comparison via a Bland–Altman diagram, in which for each  $MTR_{\text{asym}}$  (3.5 ppm) value, the difference of results obtained with both sequences is plotted versus the mutual mean. For this purpose, a ROI was created in slice 7, covering parts of WM, deeper GM and tumor tissue, as indicated by the red shaded area. The broad distribution of the mutual mean values on the x-axis represents WM and deeper GM on the left, and tumor on the right. The mean difference ( $M_D$ ) is almost zero ( $M_D = -0.007$ ), indicating almost identical CEST contrasts for both sequences. In addition, the majority of the differences on the y-axis occur within the 95% confidence interval range ( $-0.021/+0.005$ ), which is smaller than the expected CEST effect via  $MTR_{\text{asym}}$  of 0.03–0.05. This criterion does not apply to the 7% of differences outside the confidence interval, due to residual artifacts induced by partial volume effects. A correlation between both methods in the selected ROI reveals good agreement between both sequences and no significant differences ( $r = 0.86, p < .001$ ).

In addition, to check whether the contrast is preserved between tumor and WM or GM, Figure 6B shows  $MTR_{\text{asym}}$  values for the respective tissue types. Comparable distributions and median values are shown for both sequences.

## 4 | DISCUSSION

In this study, a novel and fast scheme for APT-CEST multislice imaging was proposed to speed up measurement time by almost 50%, comprising a CEST saturation and an acquisition module. The CEST saturation part includes a basic module, embedded in a loop with  $N_{\text{dummy}}$  repetitions, consisting of a rectangular saturation pulse of 250 ms duration (the longest pulse duration that was feasible on the respective MR system) followed by a delay of the same duration. The delay includes a crusher gradient followed by a FS module. The acquisition module is similar to the CEST saturation module, but contains a single-slice EPI acquisition after previous FS during the delay time. While the CEST saturation module is used to



**FIGURE 6** Bland–Altman plot for data within a ROI consisting of white matter (WM), deeper gray matter (GM) and tumor tissue to investigate the correspondence between both sequences. While the mean value of the differences is close to zero (black line), 93% of the data are located within the confidence interval, which is two times the standard deviation (red lines)

achieve the steady-state magnetization for the first frequency offset  $\omega$ , the acquisition module maintains this state and performs the recording of several slices and adjacent frequency offsets. Thus, the CEST saturation module can be omitted for further Z-spectrum acquisition, which reduces the measurement time.

Previous research has already shown that it is uncritical to subdivide a long saturation pulse with a duration of 2–4 s into several short pulses that complement each other in sum.<sup>13,26</sup> Based on a duty cycle of 50% used in this study, the CEST effect would be initially reduced, so the steady-state and therefore also the APT-CEST effect gradually build up with each saturation pulse. It is also possible to acquire multiple slices, since the CEST effect increases with each additional pulse per slice. However, the first few slices may be discarded as the steady state has not yet been fully reached. Since this effect also depends on the sequence parameters, initial experiments were performed based on the CEST<sub>SS</sub> sequence with an additional relaxation delay of 10 s, which is almost similar to the method proposed by Sun et al.<sup>10</sup> As a minimum, eight saturation pulses with a duration of 250 ms each were sufficient to achieve the steady state for the maximum tested  $T_1$  of 1300 ms. To account for the increased tumor  $T_1$ , the number of saturation pulses was doubled from  $N_{\text{dummy}} = 8$  (duration = 4 s) to  $N_{\text{dummy}} = 16$  (duration = 8 s). Further, the optimal  $B_1$  lay between 0.9 and 1.2  $\mu\text{T}$  (Figures S.1 and S.2). While lower  $B_1$  values led to an inferior saturation efficiency  $\alpha$ , higher  $B_1$  caused a broadening of the saturation peak of the amides in the Z-spectrum, accompanied by increased direct water saturation and thus a reduction of  $\text{MTR}_{\text{asym}}$  values.<sup>27,28</sup> Therefore, a  $B_1$  of 1  $\mu\text{T}$  was chosen, yielding a saturation efficiency  $\alpha$  of approximately 99%. This irradiation power has also been recommended for APT-CEST tumor imaging at 3 T to achieve the maximum contrast.<sup>29</sup>

The in vitro results showed a perfect correlation of the Z-spectra obtained with both CEST<sub>SS</sub> sequences (with and without relaxation delay). Although the acquisition for each new frequency offset did not start with a completely relaxed spin system in the case of CEST<sub>SS</sub> without relaxation delay, the data show that the achievement of full spin relaxation via adding a relaxation delay of 10 s does not affect the steady-state saturation and is therefore not required. Further, the Z-spectra show good agreement with the Z-spectra obtained with the CEST<sub>fast</sub> sequence, indicating that the frequency-selective presaturation can be omitted when using the proposed saturation scheme.

The visual inspection of parametrized  $\text{MTR}_{\text{asym}}$  (3.5 ppm) maps revealed a good contrast in vitro as well as in vivo for tumor tissue versus WM for both sequences, without any significant differences between sequences in the subtraction maps. Residual contrast differences, in voxels containing CSF, were probably due to poor motion correction and a slow drift in scanner hardware, considering the total scanning time of 48 min 24 s. According to the manufacturer, the drift of the static magnetic field of the MR system used for this study is relatively low when using an EPI sequence. For a quantitative assessment, the method proposed by Windschuh et al. was applied, performing a linear interpolation between two  $B_0$  maps, which were acquired at different time points.<sup>30</sup> In our study, the time difference between both images was 16 min, yielding an average drift of about 0.25 Hz/min within a VOI across the WM and GM. The resulting signal drift during the total measurement time of the sequence comparison (~48 min) was thus about 12 Hz (0.1 ppm), which can be deemed to be negligible.

However, motion-induced variations in CSF partial volumes at a spatial resolution of  $3 \times 3 \times 4 \text{ mm}^3$  will have a noticeable impact on the subtraction maps. This might also explain the increased differences near the cortical structures (Figures 4 and 5).

In addition, Figure 5B shows higher  $\text{MTR}_{\text{asym}}$  differences ( $>0.05$ ) around the frontal brain within the first four slices, resulting from magnetic field distortions in anatomic regions that are typically affected by this effect. Those susceptibility artefacts can also be seen at almost the same positions in the unsaturated reference data  $S_0$  (Figure 5C), affecting the signal level, thus leading to inaccurate local  $B_0$ -corrected values. Furthermore, it was shown in the simulation that there is a stronger pseudo-bleed-over effect for larger increments such as 0.5 ppm according to the CEST<sub>fast</sub> sequence for the first few slices, which hampers an adequate  $B_0$  correction. As a result from both effects, this inaccuracy affects the difference between both calculated  $\text{MTR}_{\text{asym}}$  maps. By excluding the first four slices, no significant differences could be found for WM and GM across the slices 5–16. Besides this artifact, the results indicate that at least 50% of the data deviated by less than 0.01 from the median value. For tumor tissue, signal differences are smaller, which might be attributed to the fact that the respective VOI represents a smaller and more well-defined area.

Furthermore, a small but consistently negative median value was found for the subtraction maps in all VOIs and almost every slice, which is also visible in the Bland–Altman plot. However, Figures 5 and 6 show that this bias is negligible, residing in the range of the observed standard deviation for the in vitro data. In addition, Figure 6B shows that the contrast between tumor tissue and WM/GM is retained with both sequences.

Since the SNR efficiency is defined as the SNR per square root of the measurement time, the proposed fast sequence would increase the efficiency by about 40% compared with the standard sequence. In this study, the signal gain was calculated based on the mean signal of the images, since both sequences generated the same background noise levels. This may be due to the use of identical EPI acquisition parameters (e.g. matrix size, receiver bandwidth, spatial resolution, phase-encoding direction). According to a previous study,<sup>31</sup> image noise levels can in fact be expected to be similar for different sequences, provided all noise-relevant parameters are identical. Examination of the sensitivities of the sequences compared via CNR analysis indicates similar values for both CEST<sub>SS</sub> sequences (CNR = 1.6). However, the CEST<sub>fast</sub> sequence has a slightly increased CNR of 1.8, which suggests a slightly improved sensitivity.

To improve the SNR and CNR, an optimization of the flip angle during the EPI acquisition might be used in future studies. Such optimization may be essential because a large flip angle significantly perturbs the CEST steady state, which may not be fully recovered under a short duration of 0.5 s between subsequent RF pulses.<sup>10</sup> In addition, a further modification of the sequence is conceivable to acquire data for a specific frequency offset several times in succession.

The sequence design allows flexible adjustment of the RF irradiation in the CEST saturation and acquisition module for increased  $T_1$  values. For example, our current sequence settings would only allow for relaxation to about 93% of the equilibrium magnetization at a  $T_1$  of 3000 ms for the TR chosen (8 s). By simply increasing the number of slices ( $N_{\text{slices}}$ ), a longer TR could be achieved while further improving the saturation efficiency  $\alpha$  with each additional slice. Apart from lengthening TR, the in-plane resolution can be further improved by increasing the matrix size, making use of the relatively long waiting time after each EPI readout. Moreover, the sequence allows the recording of certain spectral sections 50% faster compared with the conventional CEST<sub>SS</sub> sequence.

Results of the simulation show that a Z-spectrum with the interval of 0.1–0.25 ppm (~12–31 Hz) is highly suitable for the proposed sequence. Thus, for future studies, the measurement time might be further shortened by only recording necessary subranges of the Z-spectrum. In the case of a larger increment (e.g. 0.5 ppm) between the offsets, it is recommended to simply acquire more slices and exclude the first few because of insufficient saturation. Alternatively, adjusting the number of pulses to the selected increment size before switching the frequency offset will be considered for future studies. Thus, if the data are recorded at higher field strengths such as 7 T, it is suggested to adjust the increment to 30 Hz for a fine sampling. However, this will almost double the number of offsets compared with 3 T, so the measurement would take longer. Besides modifying the bandwidth of the increment, the acquisition of more slices due to longer  $T_1$  values might be a solution to compensate larger increments such as 60 Hz.

The advantage of the proposed sequence with the adjacent acquisition scheme depends on the number of points used to cover the APT-CEST region. In principle, there is no difference to the method of Sun et al.<sup>10</sup> compared with sampling just one point at +3.5 ppm and one at –3.5 ppm (which would require a robust  $B_0$  correction), while for two points around +3.5 and –3.5 ppm, we almost gain 50% when a small step size is used. With the proposed method and assuming a maximum step size of 0.2 ppm, one could divide the interval between 3 and 4 ppm by the number of averages required for sufficient accuracy (also taking into account outliers due to motion) and distribute them with equidistant increments across this interval. The total acquisition time would still match the time required for repetitive acquisition of 1 point, while the gain in accuracy due to a robust fit should at least compensate for the increased SNR obtained by repetitive sampling of just one point in the Z-spectrum.

A limitation may arise in multislice imaging, as each slice including the preceding saturation pulse requires 0.5 s, yielding a total of 8 s for each volume. In fact, any movement during volume acquisition can hamper adequate movement correction as it is applied in standard fMRI studies. However, it should be taken into account that the proposed acquisition scheme also offers the opportunity to discard heavily blurred volumes and to compensate them on the basis of data fitting.

## 5 | CONCLUSION

In summary, we have shown that the proposed fast CEST-EPI sequence (CEST<sub>fast</sub>) can be used for more rapid APT-CEST imaging. Compared with the modified conventional steady-state sequence (CEST<sub>SS</sub>), this method offers a speeding up by almost 50% while providing similar  $MTR_{\text{asym}}$  contrast.

## ACKNOWLEDGEMENT

We would like to thank Moritz Zaiss for his support in setting up the simulation.

## ORCID

Jan-Rüdiger Schüre  <https://orcid.org/0000-0002-1472-9471>

## REFERENCES

1. Zhou J, Payen JF, Wilson DA, Traystman RJ, van Zijl PCM. Using the amide proton signals of intracellular proteins and peptides to detect pH effects in MRI. *Nat Med*. 2003;9(8):1085-1090.
2. Ray KJ, Simard MA, Larkin JR, et al. Tumour pH and protein concentration contribute to the signal of amide proton transfer magnetic resonance imaging. *Cancer Res*. 2019;79(7):1343-1352.
3. Heo HY, Zhang Y, Jiang S, Lee DH, Zhou J. Quantitative assessment of amide proton transfer (APT) and nuclear Overhauser enhancement (NOE) imaging with extrapolated semisolid magnetization transfer reference (EMR) signals: II. Comparison of three EMR models and application to human brain glioma at 3 Tesla. *Magn Reson Med*. 2016;75(4):1630-1639.
4. Dou W, Lin CY, Ding H, et al. Chemical exchange saturation transfer magnetic resonance imaging and its main and potential applications in pre-clinical and clinical studies. *Quant Imaging Med Surg*. 2019;9(10):1747-1766.
5. Paech D, Dreher C, Regnery S, et al. Relaxation-compensated amide proton transfer (APT) MRI signal intensity is associated with survival and progression in high-grade glioma patients. *Eur Radiol*. 2019;29(9):4957-4967.
6. Jiang S, Zou T, Eberhart CG, et al. Predicting IDH mutation status in grade II gliomas using amide proton transfer-weighted (APT<sub>w</sub>) MRI. *Magn Reson Med*. 2017;78(3):1100-1109.
7. Schüre JR, Shrestha M, Breuer S, et al. The pH sensitivity of APT-CEST using phosphorus spectroscopy as a reference method. *NMR Biomed*. 2019;32(11):e4125.
8. Zhou J, Blakeley JO, Hua J, et al. Practical data acquisition method for human brain tumor amide proton transfer (APT) imaging. *Magn Reson Med*. 2008;60(4):842-849.

9. Varma G, Lenkinski RE, Vinogradov E. Keyhole chemical exchange saturation transfer. *Magn Reson Med*. 2012;68(4):1228-1233.
10. Sun PZ, Cheung JS, Wang E, Benner T, Sorensen AG. Fast multislice pH-weighted chemical exchange saturation transfer (CEST) MRI with Unevenly segmented RF irradiation. *Magn Reson Med*. 2011;65(2):588-594.
11. Baudrexel S, Nöth U, Schüre JR, Deichmann R. T1 mapping with the variable flip angle technique: A simple correction for insufficient spoiling of transverse magnetization. *Magn Reson Med*. 2018;79(6):3082-3092.
12. Nöth U, Shrestha M, Schüre JR, Deichmann R. Quantitative in vivo T2 mapping using fast spin echo techniques - A linear correction procedure. *Neuroimage*. 2017;157:476-485.
13. Sun PZ, Murata Y, Lu J, W X, Lo EH, Sorensen AG. Relaxation-compensated fast multislice amide proton transfer (APT) imaging of acute ischemic stroke. *Magn Reson Med*. 2008;59(5):1175-1182.
14. Zaiss M, Bachert P. Exchange-dependent relaxation in the rotating frame for slow and intermediate exchange - modeling off-resonant spin-lock and chemical exchange saturation transfer. *NMR Biomed*. 2013;26(5):507-518.
15. Preibisch C, Deichmann R. Influence of RF spoiling on the stability and accuracy of T1 mapping based on spoiled FLASH with varying flip angles. *Magn Reson Med*. 2009;61(1):125-135.
16. Wang HZ, Riederer SJ, Lee JN. Optimizing the precision in T1 relaxation estimation using limited flip angles. *Magn Reson Med*. 1987;5(5):399-416.
17. Gracien RM, Maiworm M, Brüche N, et al. How stable is quantitative MRI? - Assessment of intra- and inter-scanner-model reproducibility using identical acquisition sequences and data analysis programs. *Neuroimage*. 2020;207:116364.
18. Volz S, Nöth U, Rotarska-Jagiela A, Deichmann R. A fast B1-mapping method for the correction and normalization of magnetization transfer ratio maps at 3 T. *Neuroimage*. 2010;49(4):3015-3026.
19. Ma J. Dixon techniques for water and fat imaging. *J Magn Reson Imaging*. 2008;28(3):543-558.
20. Jenkinson M, Beckmann CF, Behrens TEJ, Woolrich MW, Smith SM. FSL. *Neuroimage*. 2012;62(2):782-790.
21. Dixon WT. Simple proton spectroscopic imaging. *Radiology*. 1984;153(1):189-194.
22. Jenkinson M, Bannister P, Brady M, Smith S. Improved optimization for the robust and accurate linear registration and motion correction of brain images. *Neuroimage*. 2002;17(2):825-841.
23. Smith SM. Fast robust automated brain extraction. *Hum Brain Mapp*. 2002;17(3):143-155.
24. Kim M, Gillen J, Landman BA, Zhou J, van Zijl PCM. Water saturation shift referencing (WASSR) for chemical exchange saturation transfer (CEST) experiments. *Magn Reson Med*. 2009;61(6):1441-1450.
25. Zhang Y, Brady M, Smith S. Segmentation of brain MR images through a hidden Markov random field model and the expectation-maximization algorithm. *IEEE Trans Med Imaging*. 2001;20(1):45-57.
26. Liu G, Ali MM, Yoo B, Griswold MA, Tkach JA, Pagel MD. PARACEST MRI with improved temporal resolution. *Magn Reson Med*. 2009;61(2):399-408.
27. Sun PZ, Van Zijl PC, Zhou J. Optimization of the irradiation power in chemical exchange dependent saturation transfer experiments. *J Magn Reson*. 2005;175(2):193-200.
28. Sun PZ, Wang Y, Dai ZZ, Xiao G, Wu R. Quantitative chemical exchange saturation transfer (qCEST) MRI--RF spillover effect-corrected omega plot for simultaneous determination of labile proton fraction ratio and exchange rate. *Contrast Media Mol Imaging*. 2014;9(4):268-275.
29. Zhao X, Wen Z, Huang F, et al. Saturation power dependence of amide proton transfer image contrasts in human brain tumors and strokes at 3 T. *Magn Reson Med*. 2011;66(4):1033-1041.
30. Windschuh J, Zaiss M, Ehses P, Lee JS, Jerschow A, Regatte RR. Assessment of frequency drift on CEST MRI and dynamic correction: application to gagCEST at 7 T. *Magn Reson Med*. 2019;81(1):573-582.
31. Shrestha M, Nöth U, Deichmann R. Improved signal-to-noise ratio in EPI sequences with highly asymmetric spin echo and highly asymmetric STEAM preparations (HASE-EPI and HASTEAM-EPI). *Magn Reson Mater Phys Biol Med*. 2019;32(5):549-558.

## SUPPORTING INFORMATION

Additional supporting information may be found online in the Supporting Information section at the end of this article.

**How to cite this article:** Schüre J-R, Pilatus U, Deichmann R, Hattingen E, Shrestha M. A fast and novel method for amide proton transfer-chemical exchange saturation transfer multislice imaging. *NMR in Biomedicine*. 2021;34:e4524. <https://doi.org/10.1002/nbm.4524>